ACS APPLIED MATERIALS & INTERFACES

www.acsami.org

Research Article

Model Metallic Glasses for Superior Electrocatalytic Performance in a Hydrogen Oxidation Reaction

Chaitanya Mahajan, Vahid Hasannaeimi, Nico Neuber, Xiaowei Wang, Ralf Busch, Isabella Gallino, and Sundeep Mukherjee*

Cite This: https://doi.org/10.1021/acsami.2c18266

Read Online

ACCESS | Metrics & More | Article Recommendations

ABSTRACT: Metallic glasses or amorphous alloys, with their excellent chemical stability, disordered atomic arrangement, and ability for thermoplastic nanostructuring, show promising performance toward a range of electrocatalytic reactions in proton-exchange membrane fuel cells. However, there are knowledge gaps and a distinct lack of understanding of the role of amorphous alloy chemistry in determining their catalytic activity. Here, we demonstrate the influence of alloy chemistry and the associated electronic structure on the hydrogen oxidation reaction (HOR) activity of a systematic series of $Pt_{42.5-x}Pd_xCu_{27}Ni_{9.5}P_{21}$ bulk metallic glasses (BMGs) with x = 0 to 42.5 at%. The HOR activity and electrochemical active surface area as a function of composition were in the form of volcano plots, with a peak around equal proportion of Pt and Pd. The lower relative electron work function and higher binding energy of the Pt core level explain the reduced charge-transfer resistance and improved electrocatalytic activity due to weakened chemisorption of protons in the mid-range composition. Density functional theory calculations show the lower free energy change and higher hydrogen adsorption density for these $Pt_{42.5-x}Pd_xCu_{27}Ni_{9.5}P_{21}$ BMGs, suggesting a synergistic effect from the presence of both noble metals, Pt and Pd.

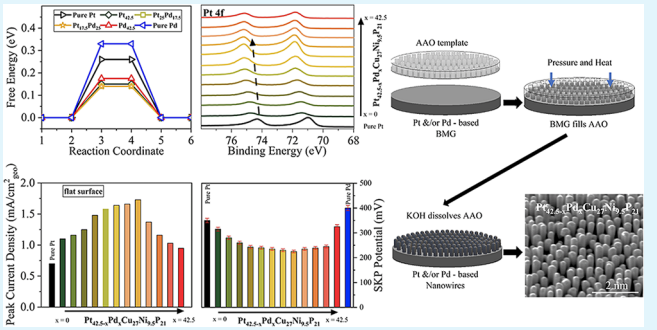

KEYWORDS: *metallic glass, fuel cell, electrocatalyst, nanowires, density functional theory*

1. INTRODUCTION

Countries around the globe are increasingly investing in clean and renewable energy sources due to environmental concerns and the impact of climate change. Hydrogen energy represents a promising route for decarbonization as it presents a platform for applications like fuel for transportation[1,2] and energy storage for heat and power generation[3,4] wherein the proton-exchange membrane fuel cells (PEMFCs) play an important role in utilizing the hydrogen energy.[5] Over the past three decades, PEMFC technology has advanced tremendously resulting in the first commercial fuel cell-powered automobile.[6] However, large-scale market penetration of this technology remains limited due to the high cost of platinum group metal (PGM) catalysts used. Over 40% cost of PEMFCs comes from PGM loading,[7] with the high cost of platinum (Pt) being the primary bottleneck for widespread adoption of these fuel cells. Therefore, higher activity of the catalyst is needed to reduce Pt usage. Substantial efforts have been devoted for enhancing the activity of PGMs like alloying with transition metals,[8,9] reducing the particle size,[10] and directed synthesis of large surface area nanostructures such as nanowires,[11] nanocages,[12] nanodendrites,[13] and nanoframes.[14] However, the nanostructure synthesis routes often suffer from limited control over catalyst morphology and length scale.[15,16]

The majority of PGM catalysts studied till date are crystalline, which favor catalytic reactions primarily along few crystallographic orientations,[17,18] thereby limiting the full potential of the catalyst. In contrast, bulk metallic glasses (BMGs) represent a new paradigm in electrocatalyst design and have shown promising performance in many catalytic reactions due to their disordered atomic structure and high density of low-coordination surface sites.[19−24] Each surface site in a metallic glass is potentially active because of atomic-scale disorders and electron localization.[25] Furthermore, BMGs have the unique appeal of facile and scalable thermoplastic manipulation at the nanometer length scale to synthesize complex hierarchical nanostructures that are attractive for catalytic applications.[23,26] Noble metal-based BMG catalysts,

Received: October 11, 2022
Accepted: January 11, 2023

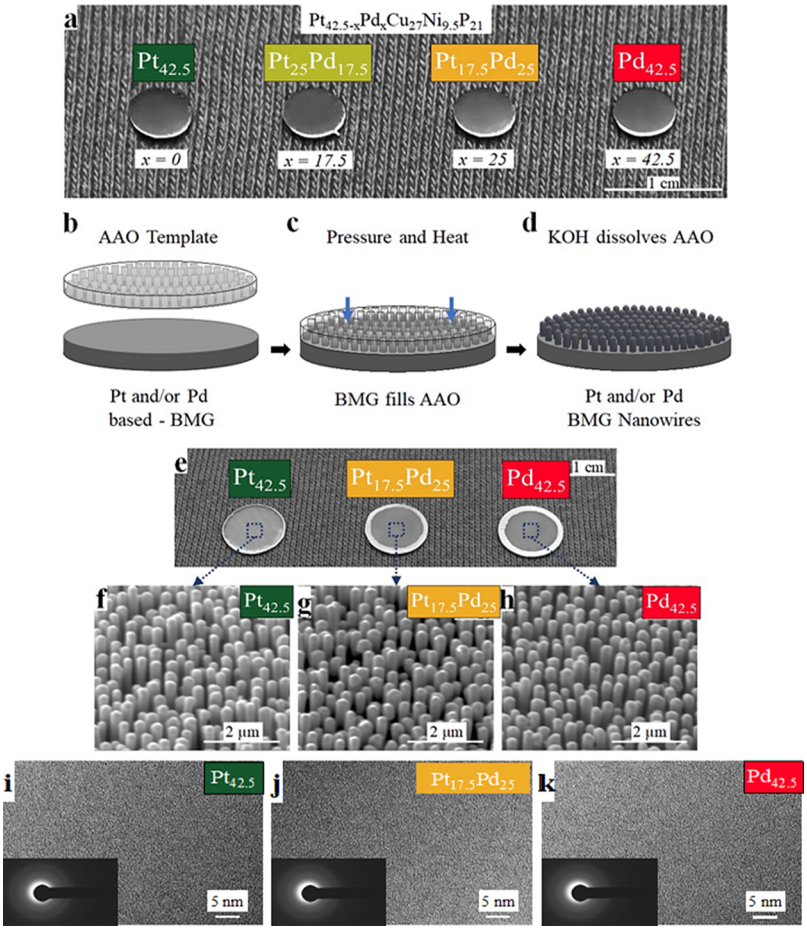

Figure 1. (a) Optical images of representative $Pt_{42.5-x}Pd_x$ alloys in the bulk form, where x = 0, 17.5, 25, and 42.5; (b–d) schematic showing TPF of BMG nanowires, where the viscous BMG flows into the AAO template under a controlled pressure and temperature; (e) optical images of the $Pt_{42.5-x}Pd_x$ BMGs after TPF with nanowires on the top surface; (f–h) SEM images of the $Pt_{42.5}$, $Pt_{17.5}Pd_{25}$, and $Pd_{42.5}$ BMG nanowires with an aspect ratio of around 5; and HRTEM images of (i) $Pt_{42.5}$, (j) $Pt_{17.5}Pd_{25}$, (k) $Pd_{42.5}$ nanowires with the SAD pattern (inset) showing diffused rings indicating a fully amorphous structure.

such as PdNiCuP,[27] PdNiPB,[22] PtCuNiP,[28] PdCuNiP,[28] and PtPdCuNiP,[29] have shown significantly higher activity compared to pure noble metals. However, there are knowledge gaps and a distinct lack of understanding of the role of BMG alloy chemistry on their catalytic activity. Fundamental understanding of these correlations will greatly help in the rational design and systematic development of next-generation electrocatalysts. In addition, there is limited understanding on the correlations between catalytic activity and electronic characteristics like binding energy and electron work function (EWF). Charge transfer during a catalytic reaction is a multistep process,[30−32] which may be related to the work function of the catalyst surface.[28,33−35] The ease of electron removal has been directly correlated with the catalyst activity in several important reactions, including hydrogen evolution, oxygen reduction, ammonia synthesis, N_2O decomposition, and soot combustion.[36−41]

In this study, the hydrogen oxidation reaction (HOR) response of a systematic series of $Pt_{42.5-x}Pd_xCu_{27}Ni_{9.5}P_{21}$ BMGs was evaluated, where platinum was systematically replaced by topologically equivalent palladium atoms. Bulk electrochemical studies were combined with scanning kelvin probe (SKP) and scanning electrochemical microscopy (SECM) for obtaining insights into the influence of electronic structure on electrocatalysis. An X-ray photoelectron spectroscopy (XPS) analysis was performed to determine the change in binding energy with the chemistry of the BMG. Furthermore, the correlations between hydrogen adsorption energy, hydrogen adsorption density, and catalytic activity were studied using density functional theory (DFT) calculations.

2. RESULTS AND DISCUSSION

2.1. Structural Characterization of the Bulk Samples and Nanowires. Representative bulk samples of $Pt_{42.5-x}Pd_x$ BMGs, 5 mm in diameter, are shown in Figure 1a that were obtained after induction melting of the ingots and tilt-casting in water-cooled copper molds under an argon atmosphere. A schematic of the thermoplastic forming (TPF) process used to obtain BMG nanowires is shown in Figure 1b–d. Commercially available anodized aluminum oxide (AAO) templates, with a pore size of 200 nm, were used for TPF at a temperature of T_g + 50 K, where T_g represents the calorimetric glass transition temperature. The BMGs were heated in their supercooled liquid region and pushed into the nanoporous templates with controlled application of 5000 N force. Figure 1e shows the optical images of the BMG samples after TPF and dissolution of the AAO templates, with free-standing nanowires attached to the BMG substrate. Scanning electron microscopy (SEM) images of the nanowires for the three alloys, namely, $Pt_{42.5}$, $Pt_{17.5}Pd_{25}$, and $Pd_{42.5}$, are shown in Figure

https://doi.org/10.1021/acsami.2c18266
ACS Appl. Mater. Interfaces XXXX, XXX, XXX−XXX

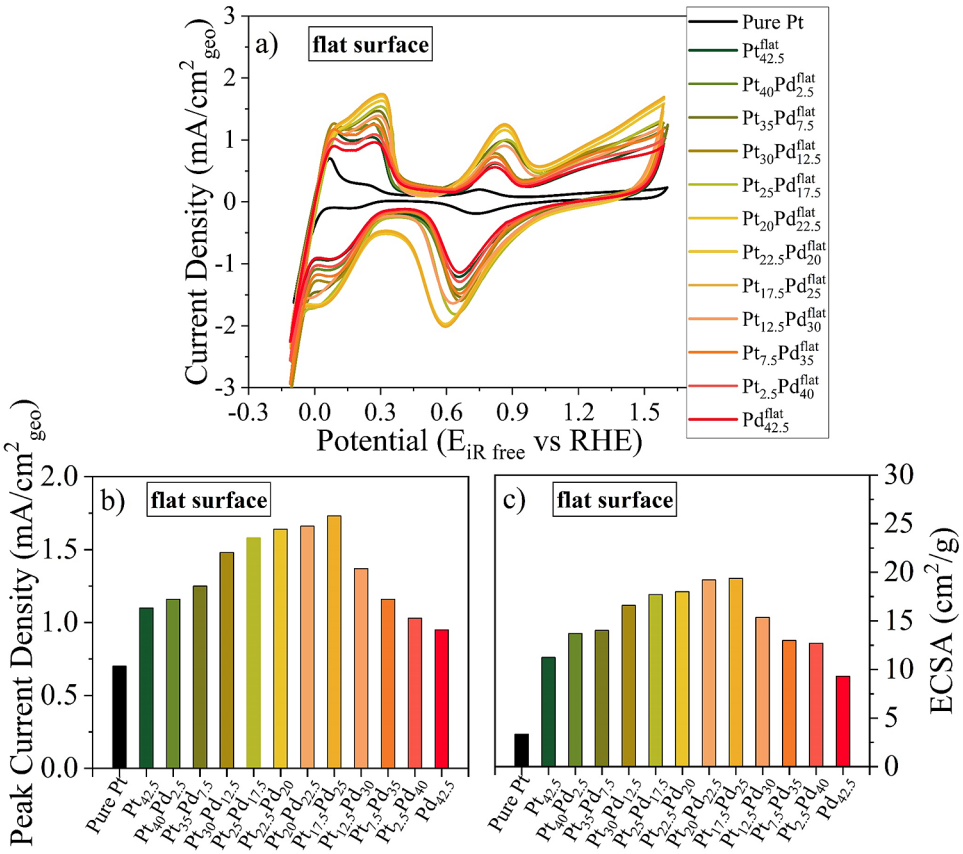

Figure 2. (a) Cyclic voltammetry (CV) curves of $Pt_{42.5-x}Pd_xCu_{27}Ni_{9.5}P_{21}$ BMGs at a scan rate of 50 mV/s, (b) peak current density in the HOR region as a function of alloy chemistry, and (c) ECSA as a function of alloy chemistry calculated from the hydrogen desorption peak in the CV curves.

1f–h. The synthesized nanowires showed on average a length of ~1 μm and a diameter of ~200 nm, indicating an aspect ratio of around 5. Figure 1i–k shows the high-resolution transmission electron microscopy (HRTEM) images of the $Pt_{42.5}$, $Pt_{17.5}Pd_{25}$, and $Pd_{42.5}$ nanowires with the diffused selected area diffraction (SAD) patterns of nanowires (insets) indicating a fully amorphous structure.

2.2. Electrochemical Characterization of the Bulk Samples and Nanowires. Figure 2a shows the cyclic polarization of the BMG flat samples in H_2-saturated 0.5 M H_2SO_4. The terminal BMGs ($Pt_{42.5}$ and $Pd_{42.5}$) showed a higher HOR activity than polycrystalline pure Pt. Furthermore, the $Pt_{42.5-x}Pd_x$ BMGs containing both Pt and Pd showed a much better performance compared to the terminal BMGs, indicating the synergistic effect from the simultaneous presence of both Pt and Pd. All the catalysts showed an onset potential of ~0 V versus RHE, demonstrating the high HOR activity. The HOR current for pure Pt increased with the applied overpotential below ~0.07 V and decreased at overpotentials greater than 0.07 V, whereas the HOR current for all the BMGs increased with the applied overpotential below 0.1 V. The $Pt_{42.5-x}Pd_x$ BMGs with x = 0, 2.5, 35, 40, and 42.5 showed two similar current peaks in the HOR region at ~0.1 and ~0.3 V. In contrast, the $Pt_{42.5-x}Pd_x$ BMGs with x = 7.5, 12.5, 17.5, 20, 22.5, 25, and 30 showed a monotonic increase in the HOR current with a limiting current at ~0.31 V. Figure 2b shows the peak current density for all the studied BMGs. The peak current density for hydrogen oxidation was significantly higher for the $Pt_{42.5-x}Pd_x$ BMGs, with the most active being $Pt_{17.5}Pd_{25}$ BMG with a peak current of 1.74 mA/cm^2. In comparison, the peak current density was 0.7, 1.13, and 0.96 mA/cm^2 for pure Pt, $Pt_{42.5}$ BMG, and $Pd_{42.5}$ BMG, respectively. The electrochemical active surface area (ECSA) was calculated to compare the catalytic activity of the different alloys as shown in Figure 2c. The ECSA was calculated by measuring the charge collected in the hydrogen adsorption/desorption region and assuming a value of 0.21 mC/cm^2 for the adsorption/desorption of a hydrogen monolayer. The ECSA can be calculated by $Q_H/(m \times 0.21)$, where m represents the loading of Pt and Pd.[42−46] The ECSA of terminal BMGs was higher by an average of three times that of pure Pt, while the catalysts with compositions around equal proportions of Pt and Pd showed a higher ECSA by a factor of ~6 compared to pure Pt and almost twice against terminal BMGs.

BMGs may be thermoplastically manipulated into complex hierarchical nanostructures. BMG nanowires represent a new architecture for fuel cell catalysts and provide facile pathways for electron transfer while offering a large surface area for catalytic reactions.[47,48] Nanowires were thermoplastically synthesized for $Pt_{42.5}$ BMG, $Pt_{17.5}Pd_{25}$ BMG, and $Pd_{42.5}$ BMG as three representative systems from the entire composition library. The HOR performance of the $Pt_{17.5}Pd_{25}$ and terminal BMG nanowires was tested under identical conditions as the flat samples. The nanowires demonstrated a significantly higher electrocatalytic activity toward HOR compared to their corresponding flat samples as shown in Figure 3a,b. Among the three alloys studied, the nanowires of the alloy with both Pt and Pd showed the highest activity. The

https://doi.org/10.1021/acsami.2c18266
ACS Appl. Mater. Interfaces XXXX, XXX, XXX−XXX

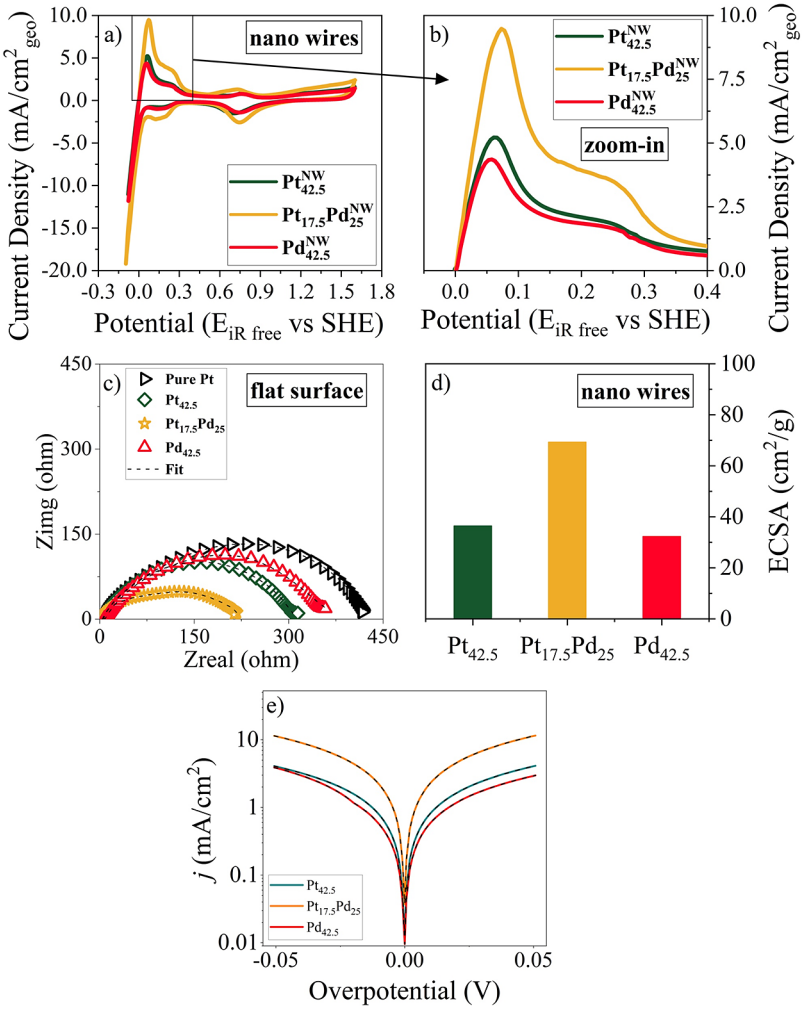

Figure 3. (a) CV curves of $Pt_{42.5}$ BMG, $Pt_{17.5}Pd_{25}$ BMG, and $Pd_{42.5}$ BMG nanowires in a H_2-saturated 0.5 M H_2SO_4 solution at a scan rate of 50 mV/s; (b) zoomed-in view of the polarization curves for the BMG nanowires; (c) EIS Nyquist plots of $Pt_{42.5}$ BMG, $Pt_{17.5}Pd_{25}$ BMG, and $Pd_{42.5}$ BMG flat samples at 39 mV overpotential; (d) ECSA calculated from the hydrogen desorption peak in the CV curves of the BMG nanowires; and (e) HOR/hydrogen evolution reaction (HER) polarization plots recorded at 2 mV/s. The Butler–Volmer fits are indicated as black dashed lines.

$Pt_{17.5}Pd_{25}$ BMG nanowire showed a HOR peak current density of 9.5 mA/cm$^2_{geo}$, which is ~five times higher compared to its corresponding flat sample and two times that of the $Pt_{42.5}$ and $Pd_{42.5}$ BMG nanowires. The superior HOR activity observed for $Pt_{17.5}Pd_{25}$ BMG is explained by the electrochemical impedance spectroscopy (EIS) measurements, which showed the smallest charge-transfer resistance for $Pt_{17.5}Pd_{25}$ compared to $Pt_{42.5}$ BMG and $Pd_{42.5}$ BMG at 29 mV overpotential (Figure 3c). The ECSA of $Pt_{17.5}Pd_{25}$ BMG nanowires was on average higher by a factor of two compared to $Pt_{42.5}$ and $Pd_{42.5}$ BMG nanowires, which is similar to the ratio for the flat samples (Figure 3d). The BMG nanowire showed higher ECSA by three times than the geometrically flats BMGs, demonstrating the enhanced activity by geometric manipulation of these BMGs. The polarization curves (Figure 3e) were fitted with a Butler–Volmer equation to obtain the exchange current density (j^0) values:

$$j = j^0 \times (e^{aF\eta/RT} - e^{-(1-a)F\eta/RT}) \quad (1)$$

where η is the overpotential, a is the transfer coefficient, T is the temperature, R is the gas constant (8.314 J mol^{-1} K^{-1}), and F is the Faraday constant (96,485 C mol^{-1}). The exchange current density follows the order $Pt_{17.5}Pd_{25}$ (2.4 mA/cm^2) > $Pt_{42.5}$ (1.1 mA/cm^2) > $Pd_{42.5}$ (0.8 mA/cm^2).

2.3. SECM and SKP Measurements for Correlating with EWF. To further elucidate the difference in electrocatalytic activity among the BMGs, the performance of the $Pt_{42.5-x}Pd_x$ alloys was compared with those of pure Pt and pure Pd using high-resolution SECM. Identical conditions of the electrolyte, temperature, and exposed surface area were maintained for all the samples. To minimize any variation related to the experimental factors, all the samples were mounted side by side on a hard resin and were tested in the same run, as shown schematically in Figure 4a. The HOR performance was studied in a 0.5 M H_2SO_4 solution identical to the CV studies. No overpotential was applied to the substrate during the experiment. Polarization between −1.2 and 0.1 V (vs $E_{Ag/AgCl}$) at the SECM tip was performed in the bulk solution at a scan rate of 50 mV/s. Due to the overpotential of the SECM tip for HER, the significant cathodic current was not observed till −0.8 V. Approach curves were measured for the metallic glass alloys and neighboring nonconductive areas to optimize the tip/substrate separation. The substrate and SECM tip were held at the open-circuit potential and −1.2 V, respectively. Positive feedback was seen

https://doi.org/10.1021/acsami.2c18266
ACS Appl. Mater. Interfaces XXXX, XXX, XXX−XXX

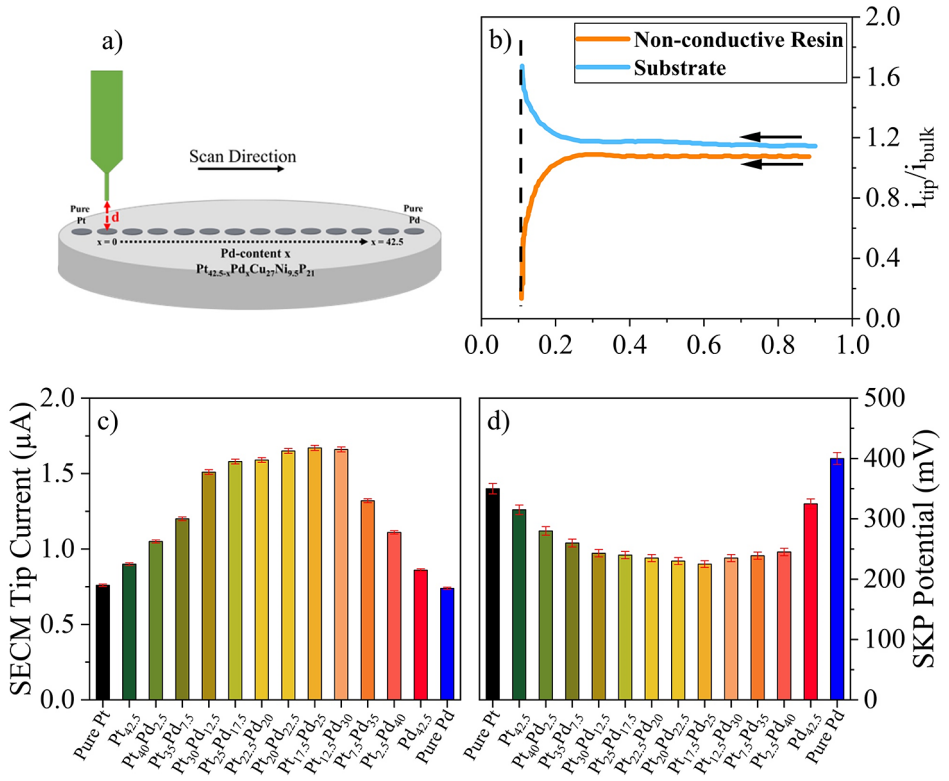

Figure 4. (a) Schematic of the experimental setup for SECM (d = 5 μm) and SKP (d = 50 μm) measurements, showing the array of $Pt_{42.5-x}Pd_x$ BMGs and pure Pt and pure Pd mounted side by side in a nonconductive resin; (b) Z-approach curves of a Pt ultramicroelectrode (UME) over a BMG surface and nonconductive resin, the dashed line shows the selected tip/substrate distance; (c) reduction current for $Pt_{42.5-x}Pd_x$ BMGs in a 0.5 M H_2SO_4 solution and tip potential held fixed at −1.2 V (vs Ag/AgCl); and (d) SKP potential for the $Pt_{42.5-x}Pd_x$ BMGs compared to pure Pt and pure Pd.

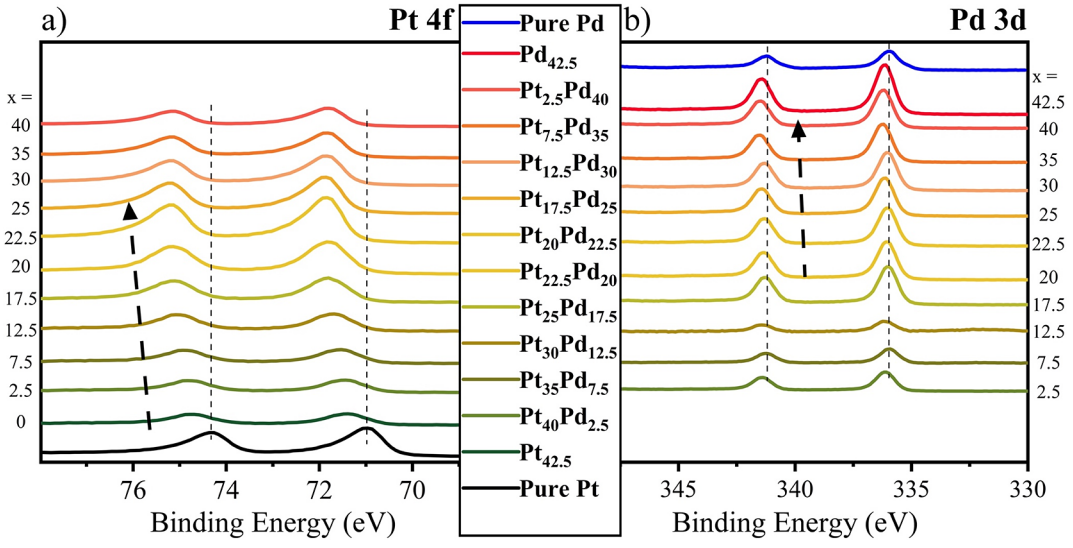

Figure 5. XPS spectra of (a) Pt 4f and (b) Pd 3d for the $Pt_{42.4-x}Pd_xCu_{27}Ni_{9.5}P_{21}$ BMGs in comparison with pure Pt and pure Pd.

when the SECM tip approached the metallic glass alloy, while negative feedback was seen for the nonconductive resin. A representative approach curve is shown in Figure 4b for $Pd_{42.5}$ BMG. The maximum SECM tip current was observed at ∼5 μm tip/substrate separation. The SECM tip was polarized at −1.2 V to have appreciable reduction of protons and scanned over each of the alloys at a fixed separation of 5 μm. The SECM tip current is proportional to the rate of catalysis, and a more negative current corresponds to the higher activity of the alloy. The average SECM tip current was measured for all the $Pt_{42.5-x}Pd_x$ BMG flat samples along with pure Pt and pure Pd discs (Figure 4c). The $Pt_{42.5}$ and $Pd_{42.5}$ BMGs showed on average ∼20% higher SECM current compared to pure Pt and Pd flat samples. The SECM tip current for $Pt_{17.5}Pd_{25}$ BMG was roughly two times that of a pure Pt flat sample. The trend in catalytic activity measured using SECM is along the same lines as the bulk CV curves. The higher activity of the $Pt_{42.5-x}Pd_x$ BMGs compared to the terminal BMGs may be attributed to

https://doi.org/10.1021/acsami.2c18266
ACS Appl. Mater. Interfaces XXXX, XXX, XXX−XXX

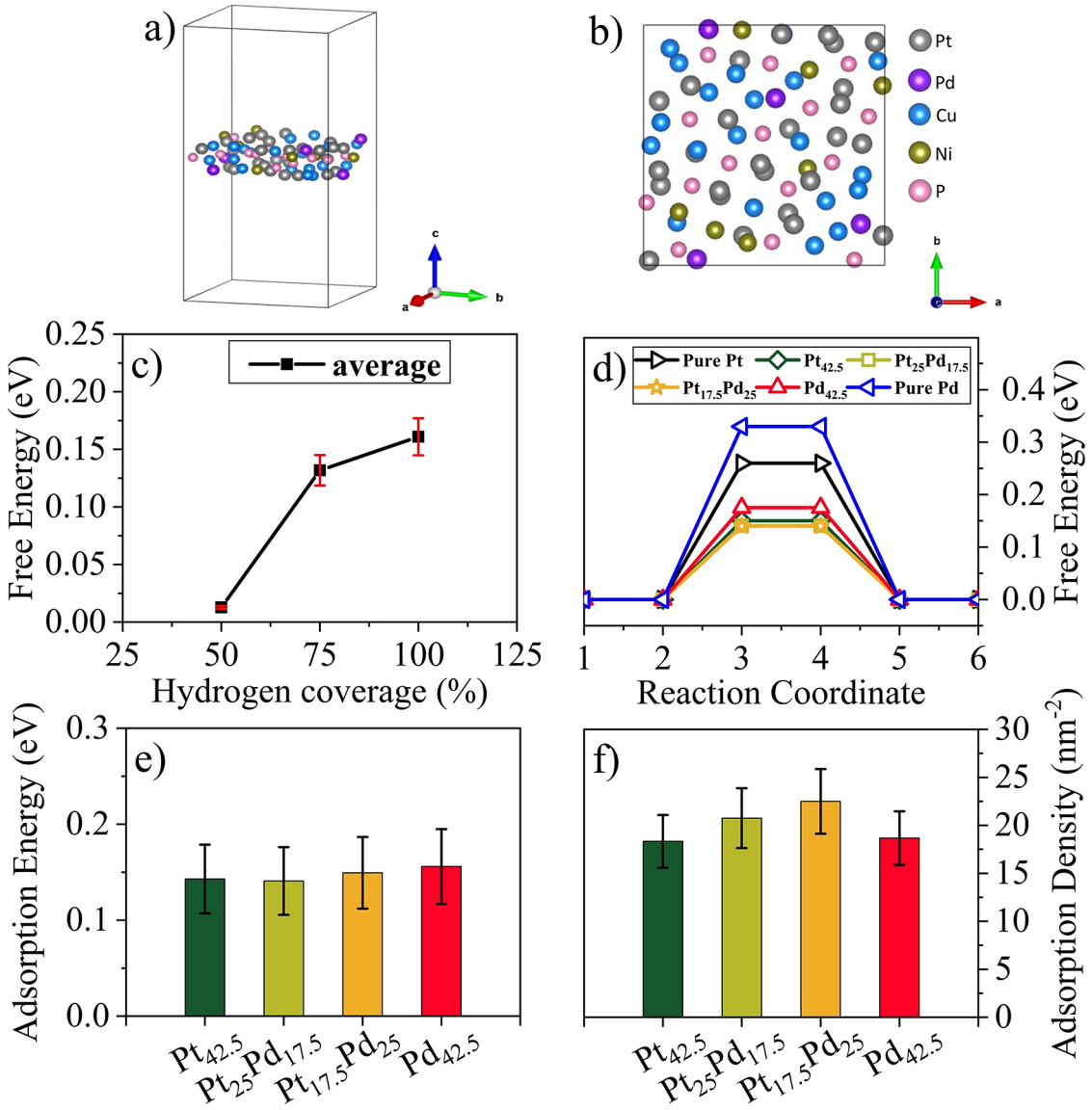

Figure 6. Schematic illustration of (a) 3D view of $Pt_{17.5}Pd_{25}$ BMG and (b) top view of $Pt_{17.5}Pd_{25}$ BMG showing the distribution of constituent atoms; (c) average free energy of hydrogen adsorption for a $Pt_{42.5-x}Pd_x$ BMG as a function of hydrogen coverage; (d) free energy diagram with the Heyrovsky−Volmer pathway for the $Pt_{42.5-x}Pd_x$ BMGs (100% hydrogen coverage) $U^{NHE} = 0$; (e) hydrogen adsorption energy (overpotential) for the $Pt_{42.5-x}Pd_x$ BMGs with 100% hydrogen coverage; and (f) hydrogen adsorption density (i.e., number of hydrogen atoms per unit area) on the surface of $Pt_{42.5-x}Pd_x$ BMGs.

the synergistic effect of Pt and Pd from electronic structure modification, which weakens the electronic interaction between the surface atoms and oxygenated species.[49] A similar synergistic effect has been demonstrated for crystalline Pd−Pt catalysts for oxygen reduction[49−52] and Pd−Au catalysts for ethanol oxidation.[53]

EWF is the minimum energy required for removing an electron from a material's surface and is a measure of the surface reactivity in redox reactions. EWF has been correlated with the surface charge-transfer process, which is an important contributing factor in electrocatalytic reactions.[31,32] The relative EWF of the systematic series of $Pt_{42.5-x}Pd_x$ BMGs was determined by measuring the SKP potential (V_{SKP}). V_{SKP} is the potential applied by the instrument to nullify the contact potential difference (V_{CPD}) between the tungsten probe and the sample. Thus, the V_{SKP} is a measure of the work function with respect to the tungsten probe ($V_{SKP} = \phi_{Tungsten} - \phi_{Sample}$).[54] Considering a constant work function of the tungsten probe, the difference in potential values was attributed to their relative EWF (relative SKP potential). An inverse correlation between the relative SKP potential and HOR activity (SECM tip current) of the $Pt_{42.5-x}Pd_x$ BMGs is shown in Figure 4c,d. The BMGs containing both Pd and Pt showed lower relative SKP potential values in comparison with Pt-based BMG and Pd-based BMG. The $Pt_{17.5}Pd_{25}$ BMG (and the immediate neighboring compositions) showed the lowest relative SKP potential and correspondingly the highest SECM tip current among the series of $Pt_{42.5-x}Pd_x$ BMGs. Thus, the superior catalytic performance toward HOR of the BMGs containing both Pt and Pd may be related to the electronic structure modification and lowering of the relative EWF, with the highest performance seen for alloys with roughly equal proportion of Pt and Pd.

https://doi.org/10.1021/acsami.2c18266
ACS Appl. Mater. Interfaces XXXX, XXX, XXX−XXX

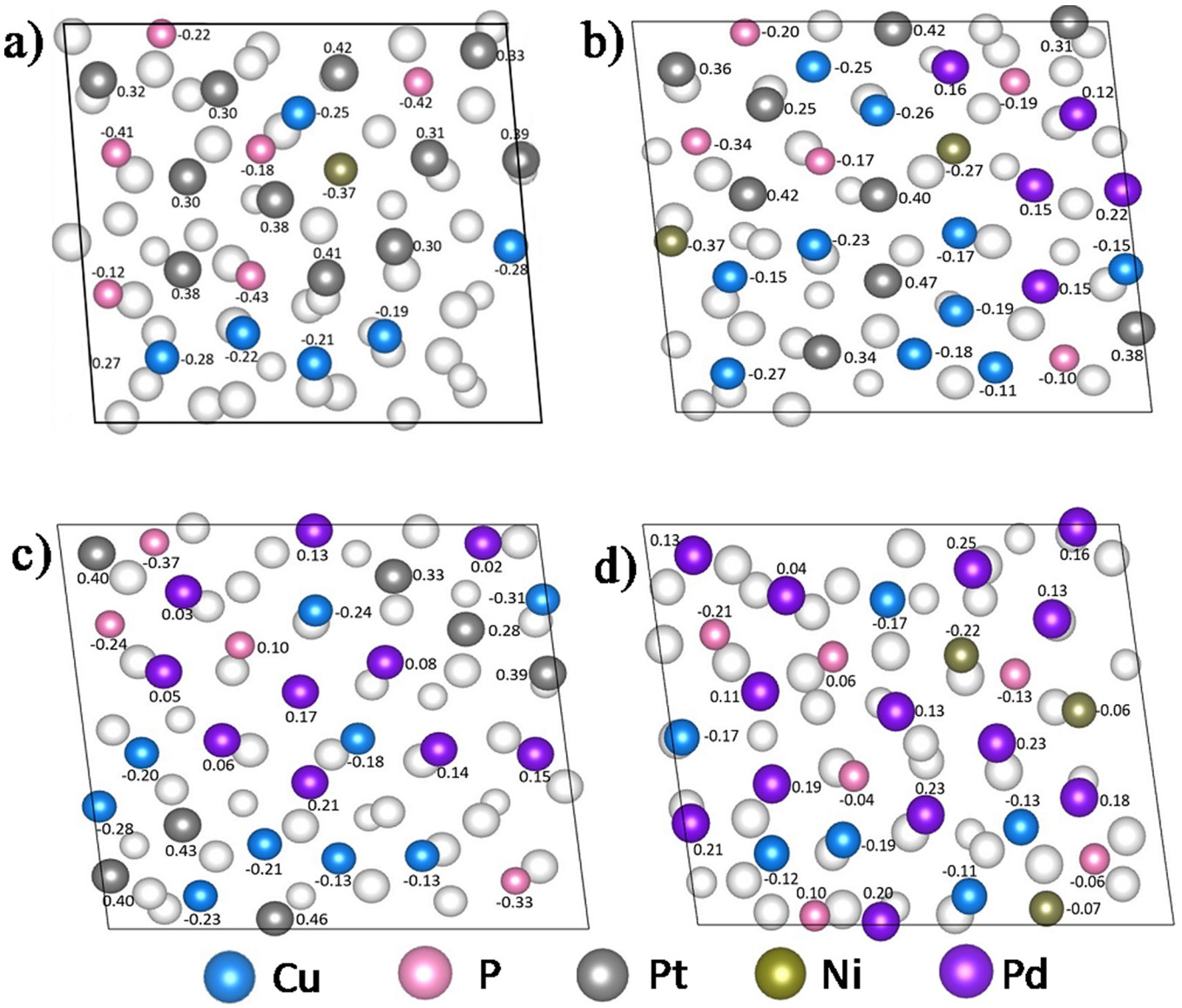

Figure 7. Surface atoms and charge distributions on the surface of $Pt_{42.5-x}Pd_xCu_{27}Ni_{9.5}P_{21}$ BMGs: (a) $x = 0$, (b) $x = 17.5$, (c) $x = 25$, and (d) $x = 42.5$. The colored and white atoms represent the surface and subsurface atoms in the alloys, respectively. Pt, Pd, Cu, Ni, and P are represented by black, purple, blue, green, and pink circles, respectively.

2.4. XPS Analysis for Correlating the Catalytic Activity with the Binding Energy. XPS was performed to characterize the surface chemical state and the recorded Pt 4f and Pd 3d core levels as shown in Figure 5a,b, respectively, for all the $Pt_{42.5-x}Pd_x$ BMGs. The core levels for Pt and Pd are separated into Pt $4f_{7/2}$, Pt $4f_{5/2}$, Pd $3d_{5/2}$, and Pd $3d_{3/2}$, respectively, due to spin−orbit splitting. The binding energy (B.E.) values at 71.3 and 74.6 eV correspond to Pt $4f_{7/2}$ and Pt $4f_{5/2}$, respectively, which are attributed to Pt^0. The absence of other Pt valence states, such as Pt^{2+}, indicates that Pt is not present in the form of oxide or hydroxide on the surface but rather in its zero-valent state. The shift in the B.E. of core levels of both Pt and Pd indicates the modification of the electronic structure with change in alloy chemistry. With an increase in the Pd content for the $Pt_{42.5-x}Pd_x$ BMGs, the B.E. of Pt and Pd showed a positive shift compared to the respective pure Pt and pure Pd binding energies. The XPS peak shifts may be correlated with the change in the *d*-band center, Fermi energy, and work function.[55,56] Usually, a positive shift in the core level B.E. is related to loss of electrons.[57−61] The positive shift of Pt and Pd core level B.Es. may be explained by partial electron transfer from less noble elements, as previously reported with alloying of Ru, Ni, Fe, Co, B, and Cu.[55,58,61,62] The shift of Pt 4f and Pd 3d core levels of our systematic series of $Pt_{42.5-x}Pd_x$ BMGs may be attributed to electron transfer from the alloying elements (Cu, Ni, and P), which is consistent with the electronegativity order. The positive shift in B.E. may be attributed to the work function difference between pure Pt and its alloy along with rehybridization of the *d*-band (valence band).[58] The change in work function, which is an upshift of the Fermi level, would result in a downshift of the core level and the valence band (*d*-band). The downshift of the *d*-band center in Pt and Pd may lead to weakened chemisorption of protons on the metallic glass surface, resulting in an enhanced catalytic activity. The B.E. of the Pt core level increases with an increase in the Pd content until $x = 25$. This trend explains the improved catalytic activity due to weakened chemisorption of

https://doi.org/10.1021/acsami.2c18266
ACS Appl. Mater. Interfaces XXXX, XXX, XXX−XXX

protons on the surface of the BMGs with an increase in the Pd content until $x = 25$ and a decrease in activity thereafter.

2.5. Theoretical Calculations. For fundamental understanding of the HOR mechanisms and to simulate the hydrogen adsorption energy and hydrogen adsorption density, molecular models of the BMGs were developed as shown in Figure 6a,b. Four models were used with different ratios of Pt/Pd ($Pt_{42.5-x}Pd_xCu_{27}Ni_{9.5}P_{21}$, x = 0, 15.4, 21.9, and 42.5) and with a nominal composition identical to some of the experimentally studied alloys. The total number of atoms for each model is 96, including Pt, Pd, Cu, Ni, and P. Each amorphous alloy cell was generated by heating to a high temperature followed by quenching and relaxation. The unoptimized cells were original with a length, width, and height of a = 13 Å, b = 13 Å, and c = 27 Å, respectively (Figure 6a). A vacuum spacing of at least 20 Å in the perpendicular z-direction (c direction, height) was employed to avert artificial interactions between the periodically repeated images. The cell parameters (length, width, and height) will slightly change once they are fully relaxed to a stable equilibrium state. For each model BMG composition, five different structures were generated to account for the stochastic nature of the distribution of surface atoms.

In an acidic environment, hydrogen oxidation may proceed via two different pathways,[63] Heyrovsky or Tafel step, followed by the Volmer step. Based on our previous work, HOR preferentially follows the Heyrovsky–Volmer pathway.[64] Since the absolute value of the free energy for hydrogen adsorption is the overpotential for HOR, the HOR catalytic activity of the BMG may be measured in terms of the hydrogen adsorption energy. From a thermodynamic viewpoint, the best catalyst is the one with the lowest overpotential for HOR. Therefore, the catalytic activity for HOR may be determined by calculating the free energy change of hydrogen desorption from the BMG surface (Volmer step). Hydrogen adsorption was simulated using DFT by introducing H atoms on the metal sites of the BMG surface. The adsorption energy was found to increase with increasing hydrogen coverage as shown in Figure 6c, which is consistent with the trend reported for pure Pt.[63] Since HOR typically proceeds under high proton coverage, ~100% hydrogen coverage was considered. Figure 6d shows the free energy change for the overall HOR process (Heyrovsky–Volmer pathway) with full hydrogen adsorption for the model BMGs in comparison to pure Pt and pure Pd. The free energy for the BMGs was significantly lower than that of pure Pt or pure Pd, which may explain their experimentally observed high catalytic activity toward HOR. To further understand the effect due to change in the Pd content in the $Pt_{42.5-x}Pd_x$ BMGs, four compositions (x = 0, 17.5, 25, and 42.5 at. %) were selected to perform the adsorption energy studies and Bader charge analysis. Five different structures of each model $Pt_{42.5-x}Pd_x$ BMG composition were calculated for the adsorption energy studies. Figure 6e shows the HOR adsorption energy for the BMGs with 100% hydrogen coverage, and the values are similar for all the compositions within the margin of error. However, the hydrogen adsorption density (i.e., the number of hydrogen atoms per unit area), as shown in Figure 6f, was higher for the alloys containing both Pt and Pd. In other words, the efficiency of hydrogen adsorption is higher for $Pt_{17.5}Pd_{25}$ and $Pt_{25}Pd_{17.5}$ BMGs compared to $Pt_{42.5}$ and $Pd_{42.5}$, even though the total noble metal content is the same for all four alloys.

The high catalytic activity of the PtPd-based BMGs originates from the synergistic effect between the alloying elements due to the electronic band structure modification and charge redistribution.[64] We calculated the Bader charge distribution on the BMG surfaces as shown in Figure 7a–d for $Pt_{42.5}$, $Pt_{25}Pd_{17.5}$, $Pt_{17.5}Pd_{25}$, and $Pd_{42.5}$ BMGs. Here, the positive charge represents gain of an electron and negative charge denotes the loss of an electron. The Pt and Pd atoms were positively charged, while Cu, Ni, and P atoms were negatively charged. Using Bader charge analysis, we found considerable charge transfer from Cu, Ni, and P atoms to Pt and Pd atoms, which is consistent with the electronegativity order. This finding is in line with the XPS analysis that showed a positive shift in Pt and Pd core level B.Es. (Figure 5) due to electron transfer from the constituent Cu, Ni, and P atoms to the noble metals. DFT calculations show that the free energy of the mid-range $Pt_{42.5-x}Pd_x$ BMGs is lower than that of the terminal compositions ($Pt_{42.5}$ BMG and $Pd_{42.5}$ BMG) and the adsorption density for the mid-range BMGs is more than 20% higher than that for the terminal compositions. Thus, the lower free energy and higher hydrogen adsorption density likely contribute to the higher catalytic activity for the mid-range composition around equal proportion of Pt and Pd in the systematic series of $Pt_{42.5-x}Pd_x$ BMGs.

3. CONCLUSIONS

The HOR activity of a systematic series of $Pt_{42.5-x}Pd_x$ BMGs (namely, $Pt_{42.5-x}Pd_xCu_{27}Ni_{9.5}P_{21}$) was studied using CV and SECM. The HOR activity and ECSA as a function of composition were in the form of volcano plots with the peak around equal proportion of Pt and Pd. Nanowires with an average length of ~1 μm and a diameter of ~200 nm were successfully synthesized for select compositions by the TPF process using commercially available AAO nanotemplates. The relative EWF of the BMGs, determined using SKP, showed an inverse correlation with the HOR activity. The XPS analysis showed a positive shift in the B.E. of the Pt core level with an increasing Pd content due to electron transfer from the constituent non-noble elements to the noble metals. The increasing B.E. of the Pt core level with maximum at $Pt_{17.5}Pd_{25}$ BMG explains the improved activity due to weakened chemisorption of protons.

The Gibbs's free energy change for hydrogen adsorption was calculated using DFT for molecular models with compositions identical to the experiments. The free energy change for the overall HOR process (Heyrovsky–Volmer pathway) with full hydrogen coverage for the mid-range compositions was significantly lower than those for the terminal compositions ($Pt_{42.5}$ BMG and $Pd_{42.5}$ BMG), pure Pt, and pure Pd. In addition, the hydrogen adsorption density for the mid-range compositions was more than 20% higher than that for the terminal compositions. The Bader charge analysis suggests electron transfer from the non-noble constituents (Cu, Ni, and P) to Pt and Pd, which is consistent with the shifts in B.E. observed from the XPS analysis. In summary, the synergy between Pt and Pd atoms in $Pt_{42.5-x}Pd_x$ BMGs resulted in a higher activity due to weakened chemisorption of hydrogen on the surface of these amorphous alloys.

4. MATERIALS AND METHODS

4.1. Materials and Characterization. A systematic series of PtPd-based BMGs was prepared with a nominal composition of $Pt_{42.5-x}Pd_xCu_{27}Ni_{9.5}P_{21}$, where x = 0, 2.5, 7.5, 12.5, 17.5, 20, 22.5, 25,

https://doi.org/10.1021/acsami.2c18266
ACS Appl. Mater. Interfaces XXXX, XXX, XXX–XXX

30, 35, 40, and 42.5 at. %, as reported recently.[65,66] The total noble metal content (i.e., Pt + Pd) was kept constant at 42.5 at% for all the alloys. In this study, the specific alloys will be referred to by their Pt and Pd contents, for example, $Pt_{30}Pd_{12.5}$ ($Pt_{42.5-x}Pd_x$) for $Pt_{30}Pd_{12.5}Cu_{27}Ni_{9.5}P_{21}$ ($Pt_{42.5-x}Pd_xCu_{27}Ni_{9.5}P_{21}$) since the amount of the other three constituents (Cu, Ni, and P) remains the same for all the alloys. $Pt_{42.5}Cu_{27}Ni_{9.5}P_{21}$ ($Pt_{42.5}$) and $Pd_{42.5}Cu_{27}Ni_{9.5}P_{21}$ ($Pd_{42.5}$) will be referred to as the terminal compositions. TPF was utilized to make nanowires for three representative alloys, namely, $Pt_{17.5}Pd_{25}$ and the two terminal compositions. The AAO templates were dissolved in a KOH solution to expose the BMG nanowires attached to the BMG substrate. The nanowires were characterized by SEM (FEI Quanta ESEM 200) and transmission electron microscopy (FEI Tecnai G2 TF20). XPS (PHI 5000 VersaProbe) was utilized to analyze the surface valence state of the alloys using flat samples, and binding energies were calibrated based on the C 1s peak value at 284.6 eV.

4.2. Electrochemical Measurements. *4.2.1. CV.* CV was used for measuring the electrocatalytic performance of the BMGs in a standard three-electrode cell using a potentiostat/galvanostat (Gamry Ref 3000) with a carbon rod as the counter electrode and a saturated calomel electrode as the reference. All the CVs were performed in a H_2-saturated 0.5 M H_2SO_4 electrolyte with a scan rate of 50 mV/s at room temperature.

4.2.2. SECM. For a side-by-side evaluation of the catalytic activity of all the BMGs in the same experimental setup, a high-resolution SECM (VersaSCAN, Ametek) was used in the redox competition mode. The main module of the system is comprised of a potentiostat (VersaSTAT 3F) attached with a linear variable differential transformer positioning system, a UME, and alloys as working electrodes. To eliminate any variability associated with the electrolyte and other experimental factors, all the alloys were scanned and monitored in a single run. All the alloys were mounted on a hard resin and were mechanically polished up to 0.1 μm followed by Vibromet polishing in a 0.04 μm colloidal silica suspension for 24 h. An Ag/AgCl (3 M) electrode (E = 0.196 V vs SHE) and a Pt wire were used as the reference and counter electrodes, respectively. A Pt/Ir (80/20) UME with a diameter of 10 μm surrounded with a borosilicate glass tube was used as the SECM tip. The tip/sample separation was optimized to 5 μm and kept constant using software-based tilt correction. Scans with a step size of 10 μm were recorded using the polarized UME over the surface of the alloys.

4.2.3. Scanning Kelvin Probe (SKP). An SKP (VersaSCAN, Princeton Applied Research) was utilized to measure the relative EWF for each of the alloys in dry lab air. A pure tungsten microprobe (250 μm in diameter) was used as a reference electrode vibrating at a frequency of 80 Hz with an amplitude of 30 μm normal to the surface. The high-resolution topography history of the samples was recorded using the constant height mode with a step size of 20 μm over all the samples to maintain a constant tip-to-sample separation of 50 μm during work function measurement. The work function was measured for all the alloys with a fixed step size, potential gain, time constant, and sensitivity.

4.3. Computational Model. HOR was studied by DFT calculations using the Vienna ab initio simulation package code for alloys with identical composition as the experiments. The exchange-correlation energy was calculated with gradient-corrected approximation of the Perdew–Burke–Ernzerhof functional.[67] The electron–ion interaction was described with projector augmented wave–generalized gradient approximation pseudopotentials with Hubbard U (DFT + U) corrections.[67,68] Wave functions were expanded using a plane-wave basis set with a kinetic energy cutoff of 500 eV with a Gamma k-point grid of 3 × 3 × 2 for Brillouin zone sampling for structural optimization. The self-consistent field was fully relaxed until a residual force convergence threshold of 0.01 eV/Å. A vacuum spacing of at least 20 Å in the perpendicular z-direction was employed to avert artificial interactions between the periodically repeated images. Spin polarization was considered in all calculations. The above parameters were optimized until the energy change was negligible.

AUTHOR INFORMATION

Corresponding Author

Sundeep Mukherjee − *Department of Materials Science and Engineering, University of North Texas, Denton, Texas 76203, United States;* orcid.org/0000-0002-1954-0045; Phone: 940-565-4170; Email: sundeep.mukherjee@unt.edu; Fax: 940-565-2944

Authors

Chaitanya Mahajan − *Department of Materials Science and Engineering, University of North Texas, Denton, Texas 76203, United States;* orcid.org/0000-0002-9490-2181

Vahid Hasannaeimi − *Department of Materials Science and Engineering, University of North Texas, Denton, Texas 76203, United States*

Nico Neuber − *Chair of Metallic Materials, Saarland University, Saarbrücken D-66123, Germany*

Xiaowei Wang − *Department of Materials Science and Engineering, University of North Texas, Denton, Texas 76203, United States*

Ralf Busch − *Chair of Metallic Materials, Saarland University, Saarbrücken D-66123, Germany*

Isabella Gallino − *Chair of Metallic Materials, Saarland University, Saarbrücken D-66123, Germany*

Complete contact information is available at: https://pubs.acs.org/10.1021/acsami.2c18266

Author Contributions

S.M. designed the study. C.M. and V.H. conducted the experiments, analyzed the results, and wrote the manuscript. X.W. conducted the computational modeling. N.N., R.B., and I.G. developed the alloys. All the authors contributed to the discussion of the results and revised the manuscript.

Notes

The authors declare no competing financial interest.

ACKNOWLEDGMENTS

S.M. would like to acknowledge the financial support from the National Science Foundation (NSF) under grant numbers 1561886, 1919220, and 1762545. Any opinions, findings, and conclusions expressed in this paper are those of the authors and do not necessarily reflect the views of the NSF. R.B. would like to acknowledge the financial support from the German Federation of Industrial Research Associations (AiF/IGF) through Project No. 21469N.

REFERENCES

(1) Jones, N. Liquid Hydrogen. *Nat. Clim. Chang.* **2012**, *2*, 23.

(2) Editorial. Hydrogen on the Rise. *Nat. Energy* **2016**, *1*, 16127.

(3) Zakeri, B.; Syri, S. Electrical Energy Storage Systems: A Comparative Life Cycle Cost Analysis. *Renew. Sustain. Energy Rev.* **2015**, *42*, 569–596.

(4) Evans, A.; Strezov, V.; Evans, T. J. Assessment of Utility Energy Storage Options for Increased Renewable Energy Penetration. *Renew. Sustain. Energy Rev.* **2012**, *16*, 4141–4147.

(5) Fan, J.; Chen, M.; Zhao, Z.; Zhang, Z.; Ye, S.; Xu, S.; Wang, H.; Li, H. Bridging the Gap between Highly Active Oxygen Reduction Reaction Catalysts and Effective Catalyst Layers for Proton Exchange Membrane Fuel Cells. *Nat. Energy* **2021**, *6*, 475–486.

(6) Yoshida, T.; Kojima, K. Toyota MIRAI Fuel Cell Vehicle and Progress toward a Future Hydrogen Society. *Electrochem. Soc. Interface* **2015**, *24*, 45–49.

(7) Thompson, S. T.; Papageorgopoulos, D. Platinum Group Metal-Free Catalysts Boost Cost Competitiveness of Fuel Cell Vehicles. *Nat. Catal.* **2019**, *2*, 558−561.
(8) Huang, X.; Zhao, Z.; Cao, L.; Chen, Y.; Zhu, E.; Lin, Z.; Li, M.; Yan, A.; Zettl, A.; Wang, Y. M.; Duan, X.; Mueller, T.; Huang, Y. High-Performance Transition Metal-Doped Pt3Ni Octahedra for Oxygen Reduction Reaction. *Science* **2015**, *348*, 1230−1234.
(9) Greeley, J.; Stephens, I. E. L.; Bondarenko, A. S.; Johansson, T. P.; Hansen, H. A.; Jaramillo, T. F.; Rossmeisl, J.; Chorkendorff, I.; Nørskov, J. K. Alloys of Platinum and Early Transition Metals as Oxygen Reduction Electrocatalysts. *Nat. Chem.* **2009**, *1*, 552−556.
(10) Debe, M. K. Electrocatalyst Approaches and Challenges for Automotive Fuel Cells. *Nature* **2012**, *486*, 43−51.
(11) Sekol, R. C.; Kumar, G.; Carmo, M.; Gittleson, F.; Hardesty-Dyck, N.; Mukherjee, S.; Schroers, J.; Taylor, A. D. Bulk Metallic Glass Micro Fuel Cell. *Small* **2013**, *9*, 2081−2085.
(12) Tian, X.; Zhao, X.; Su, Y. Q.; Wang, L.; Wang, H.; Dang, D.; Chi, B.; Liu, H.; Hensen, E. J. M.; Lou, X. W.; Xia, B. Y. Engineering Bunched Pt-Ni Alloy Nanocages for Efficient Oxygen Reduction in Practical Fuel Cells. *Science* **2019**, *366*, 850−856.
(13) Lim, B.; Jiang, M.; Camargo, P. H. C.; Cho, E. C.; Tao, J.; Lu, X.; Zhu, Y.; Xia, Y. Pd-Pt Bimetallic Nanodendrites with High Activity for Oxygen Reduction. *Science* **2009**, *324*, 1302−1305.
(14) Stephens, I. E. L.; Rossmeisl, J.; Chorkendorff, I. Toward Sustainable Fuel Cells. *Science* **2016**, *354*, 1378−1379.
(15) Porel, S.; Hebalkar, N.; Sreedhar, B.; Radhakrishnan, T. P. Palladium Nanowire from Precursor Nanowire: Crystal-to-Crystal Transformation via In Situ Reduction by Polymer Matrix. *Adv. Funct. Mater.* **2007**, *17*, 2550−2556.
(16) Xiong, Y.; Chen, J.; Wiley, B.; Xia, Y.; Aloni, S.; Yin, Y. Understanding the Role of Oxidative Etching in the Polyol Synthesis of Pd Nanoparticles with Uniform Shape and Size. *J. Am. Chem. Soc.* **2005**, *127*, 7332−7333.
(17) Adžić, R. R.; Tripkoviá, A. v.; O'grady, W. E. Structural Effects in Electrocatalysis. *Nature* **1982**, *296*, 137−138.
(18) Kobayashi, S.; Wakisaka, M.; Tryk, D. A.; Iiyama, A.; Uchida, H. Effect of Alloy Composition and Crystal Face of Pt-Skin/Pt100-XCox [(111), (100), and (110)] Single Crystal Electrodes on the Oxygen Reduction Reaction Activity. *J. Phys. Chem. C* **2017**, *121*, 11234−11240.
(19) Carmo, M.; Sekol, R. C.; Ding, S.; Kumar, G.; Schroers, J.; Taylor, A. D. Bulk Metallic Glass Nanowire Architecture for Electrochemical Applications. *ACS Nano* **2011**, *5*, 2979−2983.
(20) Mukherjee, S.; Sekol, R. C.; Carmo, M.; Altman, E. I.; Taylor, A. D.; Schroers, J. Tunable Hierarchical Metallic-Glass Nanostructures. *Adv. Funct. Mater.* **2013**, *23*, 2708−2713.
(21) Sadeghilaridjani, M.; Yang, Y. C.; Hasannaeimi, V.; Mahajan, C.; Jha, S.; Pole, M.; Xia, Z.; Mukherjee, S. Multiscale Manufacturing of Amorphous Alloys by a Facile Electrodeposition Approach and Their Property Dependence on the Local Atomic Order. *ACS Appl. Mater. Interfaces* **2021**, *13*, 9260−9271.
(22) Mukherjee, S.; Carmo, M.; Kumar, G.; Sekol, R. C.; Taylor, A. D.; Schroers, J. Palladium Nanostructures from Multi-Component Metallic Glass. *Electrochim. Acta* **2012**, *74*, 145−150.
(23) Kumar, G.; Tang, H. X.; Schroers, J. Nanomoulding with Amorphous Metals. *Nature* **2009**, *457*, 868−872.
(24) Li, J.; Doubek, G.; McMillon-Brown, L.; Taylor, A. D. Recent Advances in Metallic Glass Nanostructures: Synthesis Strategies and Electrocatalytic Applications. *Adv. Mater.* **2019**, *31*, No. 1802120.
(25) Hasannaeimi, V.; Wang, X.; Salloom, R.; Xia, Z.; Schroers, J.; Mukherjee, S. Nanomanufacturing of Non-Noble Amorphous Alloys for Electrocatalysis. *ACS Appl. Energy Mater.* **2020**, *3*, 12099−12107.
(26) Schroers, J. Processing of Bulk Metallic Glass. *Adv. Mater.* **2010**, *22*, 1566−1597.
(27) Sekol, R. C.; Carmo, M.; Kumar, G.; Gittleson, F.; Doubek, G.; Sun, K.; Schroers, J.; Taylor, A. D. Pd−Ni−Cu−P Metallic Glass Nanowires for Methanol and Ethanol Oxidation in Alkaline Media. *Int. J. Hydrogen Energy* **2013**, *38*, 11248−11255.
(28) Hasannaeimi, V.; Mukherjee, S. Noble-Metal Based Metallic Glasses as Highly Catalytic Materials for Hydrogen Oxidation Reaction in Fuel Cells. *Sci. Rep.* **2019**, *9*, 12136.
(29) Jia, Z.; Nomoto, K.; Wang, Q.; Kong, C.; Sun, L.; Zhang, L.-C. C.; Liang, S.-X. X.; Lu, J.; Kruzic, J. J. A Self-Supported High-Entropy Metallic Glass with a Nanosponge Architecture for Efficient Hydrogen Evolution under Alkaline and Acidic Conditions. *Adv. Funct. Mater.* **2021**, *31*, No. 2101586.
(30) Pan, Z. Z.; Li, Y.; Zhao, Y.; Zhang, C.; Chen, H. Bulk Phase Charge Transfer in Focus − And in Sequential along with Surface Steps. *Catal. Today* **2021**, *364*, 2−6.
(31) Casalongue, H. S.; Kaya, S.; Viswanathan, V.; Miller, D. J.; Friebel, D.; Hansen, H. A.; Nørskov, J. K.; Nilsson, A.; Ogasawara, H. Direct Observation of the Oxygenated Species during Oxygen Reduction on a Platinum Fuel Cell Cathode. *Nat. Commun.* **2013**, *4*, 2817.
(32) Kim, J. H.; Ishihara, A.; Mitsushima, S.; Kamiya, N.; Ota, K. I. Catalytic Activity of Titanium Oxide for Oxygen Reduction Reaction as a Non-Platinum Catalyst for PEFC. *Electrochim. Acta* **2007**, *52*, 2492−2497.
(33) Rohwerder, M.; Turcu, F. High-Resolution Kelvin Probe Microscopy in Corrosion Science: Scanning Kelvin Probe Force Microscopy (SKPFM) versus Classical Scanning Kelvin Probe (SKP). *Electrochim. Acta* **2007**, *53*, 290−299.
(34) Ritty, B.; Wachtel, F.; Manquenouille, R.; Ott, F.; Donnet, J. B. Conditions Necessary to Get Meaningful Measurements from the Kelvin Method. *J. Phys. E* **1982**, *15*, 310.
(35) Imbihl, R. Electrochemical Promotion of Catalytic Reactions. *Prog. Surf. Sci.* **2010**, *85*, 241−278.
(36) Grzybek, G.; Stelmachowski, P.; Gudyka, S.; Duch, J.; Ćmil, K.; Kotarba, A.; Sojka, Z. Insights into the Twofold Role of Cs Doping on DeN2O Activity of Cobalt Spinel Catalyst—towards Rational Optimization of the Precursor and Loading. *Appl. Catal. B: Environ.* **2015**, *168-169*, 509−514.
(37) Reli, M.; Ambrožová, N.; Šihor, M.; Matějová, L.; Čapek, L.; Obalová, L.; Matžj, Z.; Kotarba, A.; Kočí, K. Novel Cerium Doped Titania Catalysts for Photocatalytic Decomposition of Ammonia. *Appl. Catal. B: Environ.* **2015**, *178*, 108−116.
(38) Kaspera, W.; Zieliński, S.; Kotarba, A. Alkali Tungsten Bronzes as Soot Oxidation Catalysts: The Key Role of Electrodonor Properties of Catalytic Surface. *Catal. Commun.* **2017**, *98*, 76−80.
(39) Trasatti, S. Work Function, Electronegativity, and Electrochemical Behaviour of Metals: II. Potentials of Zero Charge and "Electrochemical" Work Functions. *J. Electroanal. Chem. Interfacial Electrochem.* **1971**, *33*, 351−378.
(40) Trasatti, S. Work Function, Electronegativity, and Electrochemical Behaviour of Metals: III. Electrolytic Hydrogen Evolution in Acid Solutions. *J. Electroanal. Chem. Interfacial Electrochem.* **1972**, *39*, 163−184.
(41) Harinipriya, S.; Sangaranarayanan, M. V. Influence of the Work Function on Electron Transfer Processes at Metals: Application to the Hydrogen Evolution Reaction. *Langmuir* **2002**, *18*, 5572−5578.
(42) Lu, Y.; Chen, W. One-Pot Synthesis of Heterostructured Pt−Ru Nanocrystals for Catalytic Formic Acid Oxidation. *Chem. Commun.* **2011**, *47*, 2541−2543.
(43) Ran, X.; Yang, L.; Qu, Q.; Li, S.; Chen, Y.; Zuo, L.; Li, L. Synthesis of Well-Dispersive 2.0 Nm Pd−Pt Bimetallic Nanoclusters Supported on β-Cyclodextrin Functionalized Graphene with Excellent Electrocatalytic Activity. *RSC Adv.* **2017**, *7*, 1947−1955.
(44) Yang, X.; Yang, Q.; Xu, J.; Lee, C. S. Bimetallic PtPd Nanoparticles on Nafion−Graphene Film as Catalyst for Ethanol Electro-Oxidation. *J. Mater. Chem.* **2012**, *22*, 8057−8062.
(45) van Hien, H.; Thanh, T. D.; Chuong, N. D.; Hui, D.; Kim, N. H.; Lee, J. H. Hierarchical Porous Framework of Ultrasmall PtPd Alloy-Integrated Graphene as Active and Stable Catalyst for Ethanol Oxidation. *Compos. B Eng.* **2018**, *143*, 96−104.
(46) Lu, Y.; Jiang, Y.; Wu, H.; Chen, W. Nano-PtPd Cubes on Graphene Exhibit Enhanced Activity and Durability in Methanol

https://doi.org/10.1021/acsami.2c18266
ACS Appl. Mater. Interfaces XXXX, XXX, XXX−XXX

Electrooxidation after CO Stripping-Cleaning. *J. Phys. Chem. C* **2013**, *117*, 2926−2938.
(47) Yin, H.; Zhao, S.; Zhao, K.; Muqsit, A.; Tang, H.; Chang, L.; Zhao, H.; Gao, Y.; Tang, Z. Ultrathin Platinum Nanowires Grown on Single-Layered Nickel Hydroxide with High Hydrogen Evolution Activity. *Nat. Commun.* **2015**, *6*, 6430.
(48) Li, M.; Zhao, Z.; Cheng, T.; Fortunelli, A.; Chen, C. Y.; Yu, R.; Zhang, Q.; Gu, L.; Merinov, B. V.; Lin, Z.; Zhu, E.; Yu, T.; Jia, Q.; Guo, J.; Zhang, L.; Goddard, W. A.; Huang, Y.; Duan, X. Ultrafine Jagged Platinum Nanowires Enable Ultrahigh Mass Activity for the Oxygen Reduction Reaction. *Science* **2016**, *354*, 1414−1419.
(49) Kang, Y.; Ye, X.; Chen, J.; Cai, Y.; Diaz, R. E.; Adzic, R. R.; Stach, E. A.; Murray, C. B. Design of Pt−Pd Binary Superlattices Exploiting Shape Effects and Synergistic Effects for Oxygen Reduction Reactions. *J. Am. Chem. Soc.* **2013**, *135*, 42−45.
(50) Sasaki, K.; Naohara, H.; Cai, Y.; Choi, Y. M.; Liu, P.; Vukmirovic, M. B.; Wang, J. X.; Adzic, R. R. Core-Protected Platinum Monolayer Shell High-Stability Electrocatalysts for Fuel-Cell Cathodes. *Angew. Chem., Int. Ed.* **2010**, *122*, 8784−8789.
(51) Wang, J. X.; Inada, H.; Wu, L.; Zhu, Y.; Choi, Y.; Liu, P.; Zhou, W.-P.; Adzic, R. R. Oxygen Reduction on Well-Defined Core−Shell Nanocatalysts: Particle Size, Facet, and Pt Shell Thickness Effects. *J. Am. Chem. Soc.* **2009**, *131*, 17298−17302.
(52) Lee, H.; Habas, S. E.; Somorjai, G. A.; Yang, P. Localized Pd Overgrowth on Cubic Pt Nanocrystals for Enhanced Electrocatalytic Oxidation of Formic Acid. *J. Am. Chem. Soc.* **2008**, *130*, 5406−5407.
(53) Cheng, F.; Dai, X.; Wang, H.; Ping Jiang, S.; Zhang, M.; Xu, C. Synergistic Effect of Pd-Au Bimetallic Surfaces in Au-Covered Pd Nanowires Studied for Ethanol Oxidation. *Electrochim. Acta* **2010**, *55*, 2295−2298.
(54) Mahajan, C.; Hasannaeimi, V.; Pole, M.; Kautz, E.; Gwalani, B.; Mukherjee, S. Corrosion Mechanisms in Model Binary Metallic Glass Coatings on Mild Steel and Correlation with Electron Work Function. *Corros. Sci.* **2022**, *207*, No. 110578.
(55) Zhao, Q.; Zhang, G.; Xu, G.; Li, Y.; Liu, B.; Gong, X.; Zheng, D.; Zhang, J.; Wang, Q. Synthesis of Highly Active and Dual-Functional Electrocatalysts for Methanol Oxidation and Oxygen Reduction Reactions. *Appl. Surf. Sci.* **2016**, *389*, 181−189.
(56) Zhao, M.; Abe, K.; Yamaura, S. I.; Yamamoto, Y.; Asao, N. Fabrication of Pd-Ni-P Metallic Glass Nanoparticles and Their Application as Highly Durable Catalysts in Methanol Electro-Oxidation. *Chem. Mater.* **2014**, *26*, 1056−1061.
(57) Weinert, M.; Watson, R. E. Core-Level Shifts in Bulk Alloys and Surface Adlayers. *Phys. Rev. B Condens. Matter* **1995**, *51*, 17168−17180.
(58) Wakisaka, M.; Mitsui, S.; Hirose, Y.; Kawashima, K.; Uchida, H.; Watanabe, M. Electronic Structures of Pt−Co and Pt−Ru Alloys for CO-Tolerant Anode Catalysts in Polymer Electrolyte Fuel Cells Studied by EC−XPS. *J. Phys. Chem. B* **2006**, *110*, 23489−23496.
(59) Tang, J. X.; Chen, Q. S.; You, L. X.; Liao, H. G.; Sun, S. G.; Zhou, S. G.; Xu, Z. N.; Chen, Y. M.; Guo, G. C. Screw-like PdPt Nanowires as Highly Efficient Electrocatalysts for Methanol and Ethylene Glycol Oxidation. *J. Mater. Chem. A Mater.* **2018**, *6*, 2327−2336.
(60) Hu, S.; Ha, S.; Scudiero, L. Temperature Dependence Study of Pd−Cu Supported Bimetallic Films by Photoelectron Spectroscopy and Cyclic Voltammetry. *Electrochim. Acta* **2013**, *105*, 362−370.
(61) Wang, M.; Qin, X.; Jiang, K.; Dong, Y.; Shao, M.; Cai, W.-B. Electrocatalytic Activities of Oxygen Reduction Reaction on Pd/C and Pd-B/C Catalysts. *J. Phys. Chem. C* **2017**, *121*, 3416−3423.
(62) Chen, D.; Sun, P.; Liu, H.; Yang, J. Bimetallic Cu−Pd Alloy Multipods and Their Highly Electrocatalytic Performance for Formic Acid Oxidation and Oxygen Reduction. *J. Mater. Chem. A Mater.* **2017**, *5*, 4421−4429.
(63) Nørskov, J. K.; Bligaard, T.; Logadottir, A.; Kitchin, J. R.; Chen, J. G.; Pandelov, S.; Stimming, U. Trends in the Exchange Current for Hydrogen Evolution. *J. Electrochem. Soc.* **2005**, *152*, J23−J26.
(64) Hasannaeimi, V.; Lin, C.-Y.; Xia, Z.; Mukherjee, S. Hydrogen Oxidation Reaction Response of Noble-Metal Based Bulk Metallic Glasses. *Electrochim. Acta* **2020**, *353*, No. 136616.
(65) Neuber, N.; Gross, O.; Frey, M.; Bochtler, B.; Kuball, A.; Hechler, S.; Gallino, I.; Busch, R. On the Thermodynamics and Its Connection to Structure in the Pt-Pd-Cu-Ni-P Bulk Metallic Glass Forming System. *Acta Mater.* **2021**, *220*, No. 117300.
(66) Gross, O.; Neuber, N.; Kuball, A.; Bochtler, B.; Hechler, S.; Frey, M.; Busch, R. Signatures of Structural Differences in Pt−P- and Pd−P-Based Bulk Glass-Forming Liquids. *Commun. Phys.* **2019**, *2*, 1−8.
(67) Blöchl, P. E. Projector Augmented-Wave Method. *Phys. Rev. B* **1994**, *50*, 17953.
(68) Kresse, G.; Joubert, D. From Ultrasoft Pseudopotentials to the Projector Augmented-Wave Method. *Phys. Rev. B* **1999**, *59*, 1758.

https://doi.org/10.1021/acsami.2c18266
ACS Appl. Mater. Interfaces XXXX, XXX, XXX−XXX